Available online at www.sciencedirect.com
ScienceDirect
Journal of Computational Physics 217 (2006) 845–865
JOURNAL OF COMPUTATIONAL PHYSICS
www.elsevier.com/locate/jcp

Computing large-amplitude progressive Rossby waves on a sphere

T.G. Callaghan *, L.K. Forbes

School of Mathematics and Physics, University of Tasmania, GPO Box 252-37, Hobart, TAS 7001, Australia

Received 26 June 2005; received in revised form 18 January 2006; accepted 23 January 2006
Available online 20 March 2006

Abstract

We consider the flow of a thin layer of incompressible fluid on a rotating sphere, bounded internally by the surface of the sphere and externally by a free surface. Progressive-wave solutions are sought for this problem, without tangent plane simplifications. A linearized theory is derived for small amplitude perturbations about a base westerly flow field, allowing calculation of the linearized progressive wavespeed. This result is then extended to the numerical solution of the full model, to obtain highly non-linear large-amplitude progressive-wave solutions in the form of Fourier series. A detailed picture is developed of how the progressive wavespeed depends on wave amplitude. This approach reveals the presence of non-linear resonance behaviour, with different disjointed solution branches existing at different values of the amplitude. Additionally, we show that the formation of localized low pressure systems cut off from the main flow field is an inherent feature of the non-linear dynamics, once the amplitude forcing reaches a certain critical level.

Keywords: Incompressible; Shallow water equations; Progressive Rossby wave; Non-linear resonance

1. Introduction

Since the classic paper by Rossby [1], proving the existence of large scale planetary waves in the atmosphere, there has been much interest in understanding these so-called Rossby waves. In particular, how Rossby waves influence the global circulation of the atmosphere has been the focus of a wide body of research over the past 60 years and it has been suggested by Lorenz [2], and later supported by Lilly [3], that the dynamical stability of Rossby waves might impose a limit on the overall numerical predictability of the global circulation.

Traditionally, almost all analytical and numerical analysis of planetary waves has been carried out either on a localized tangent plane to a sphere, the β-plane, or else with a simplified set of governing equations for the full spherical geometry. The benefits of these two approaches are that the recovery of closed form wave solutions to the equations under consideration is often possible, of which the wave forms found by Haurwitz [4] and Longuet-Higgins [5,6] are classic examples. The present paper, following work first introduced by Haurwitz [4], makes no tangent plane simplifications and also uses the shallow water equations for a thin layer of

* Corresponding author. Tel.: +61 3 62262731; fax: +61 3 62262410.
E-mail address: tgc@hilbert.maths.utas.edu.au (T.G. Callaghan).

0021-9991/$ - see front matter
doi:10.1016/j.jcp.2006.01.035

incompressible fluid with a free surface on a rotating sphere. The aim is to incorporate the spherical geometry in the governing dynamics.

The shallow water equations have been used extensively in dynamic meteorological modelling. The paper by Williamson et al. [7] has subsequently generated a large literature of papers using the shallow water equations as a basic test bed for fast global atmospheric solver algorithms. Their test case 6 employs the Rossby–Haurwitz wave, with parameters similar to those first used by Phillips [8], to initialize the flow state which is subsequently computed at later time steps. While the Rossby–Haurwitz wave is useful here as a flow initializer it is important to remember that it is not an exact analytical solution of the full non-linear shallow water equations. Indeed, there is numerical evidence by Thuburn and Li [9] that the zonal wavenumber 4 Rossby–Haurwitz wave is dynamically unstable and will eventually break down as the result of an initial perturbation. This agrees in general with previous work conducted by Hoskins [10] and Baines [11] who both found maximum amplitudes beyond which instability of Rossby–Haurwitz waves subject to perturbations was observed. All these results serve to highlight the fact that Rossby–Haurwitz waves, while analytic solutions of the barotropic vorticity equation, are not true solutions of the shallow water equations on a sphere.

Another possible source of instability for Rossby waves could be the presence of non-linear resonances, as certain key parameters are changed. Resonances are known in the water-wave literature, and are characterized by the presence of two or more solution branches in close proximity. Resonances in large-amplitude free-surface waves were apparently first encountered by Wilton [12], in the context of gravity-capillary waves. Schwartz and Vanden-Broeck [13] and Hogan [14–16] subsequently showed that the small divisors in Wilton's resonant solutions are indeed associated with multiple solution branches. Forbes [17,18] encountered a similar phenomenon in waves beneath a floating elastic ice sheet.

In the meteorological context, non-linear resonance behaviour has been studied by Longuet-Higgins and Gill [19], who showed that long-term resonant interactions can exist between three waves, termed a resonant triad. They found an algebraic relationship relating the individual wavenumbers, associated with each physical dimension, and corresponding wavespeeds; their results are concerned with planetary waves both on the β-plane and more generally on a spherical surface. The instabilities found by both Hoskins [10] and Baines [11] extended this work by calculating amplitudes required for instability based on triad interactions for specific types of Rossby–Haurwitz waves. Thus, small perturbations to a Rossby–Haurwitz wave which has been used to initialize a numerical solution of the shallow atmosphere equations, could cause the wave to fluctuate between one solution branch and another in an unpredictable fashion, or break down structurally altogether.

In this paper, we extend the above literature by finding numerical solutions of the shallow water equations in the form of progressive waves that propagate in time without change of shape. In Section 2 we present the governing dynamical equations in dimensionless form, and a linearized model of small amplitude progressive-wave solutions to these equations is derived in Section 3. The collocation-Galerkin method for the solution of the fully non-linear system is outlined in Section 4, and results are presented, with an emphasis on wavespeed–amplitude relationships, in Section 5. A brief summary and discussion in Section 6 concludes the paper.

2. The governing equations

2.1. Equations of motion

The standard dimensional shallow water equations without topography are

$$\frac{\partial h}{\partial t}+\frac{u_\lambda}{a\cos\phi}\frac{\partial h}{\partial \lambda}+\frac{u_\phi}{a}\frac{\partial h}{\partial \phi}+\frac{h}{a\cos\phi}\left[\frac{\partial u_\lambda}{\partial \lambda}+\cos\phi\frac{\partial u_\phi}{\partial \phi}-u_\phi\sin\phi\right]=0, \tag{1}$$

$$\frac{\partial u_\lambda}{\partial t}+\frac{u_\lambda}{a\cos\phi}\frac{\partial u_\lambda}{\partial \lambda}+\frac{u_\phi}{a}\frac{\partial u_\lambda}{\partial \phi}-\left(f+\frac{u_\lambda}{a}\tan\phi\right)u_\phi+\frac{g}{a\cos\phi}\frac{\partial h}{\partial \lambda}=0, \tag{2}$$

$$\frac{\partial u_\phi}{\partial t}+\frac{u_\lambda}{a\cos\phi}\frac{\partial u_\phi}{\partial \lambda}+\frac{u_\phi}{a}\frac{\partial u_\phi}{\partial \phi}+\left(f+\frac{u_\lambda}{a}\tan\phi\right)u_\lambda+\frac{g}{a}\frac{\partial h}{\partial \phi}=0, \tag{3}$$

where (λ,ϕ,t) are longitude, latitude and time, (u_λ,u_ϕ) the corresponding velocity components, h the layer depth, a the radius of the sphere and g the gravity acceleration. The Coriolis term f is given by $f=2\Omega\sin\phi$

where Ω is the rotation rate of the sphere. These are well known as a simplified dynamical system that qualitatively mimics some aspects of real atmospheric flow (see, for instance, Gill [20]).

In so far as we are only concerned with progressive wave structures in the current work, we define a coordinate transform given by

$$\eta = \lambda - ct. \tag{4}$$

The second term $-ct$ in (4) merely translates any initial wave structure towards the East ($c > 0$) or West ($c < 0$) with constant angular speed c. Reference scales v_{ref}, h_{ref} and c_{ref} are introduced as representative characteristic values of the speed, fluid depth and progressive angular wavespeed, respectively. The dynamical equations are then non-dimensionalized, in a manner similar to that adopted by Klein [21], so that the complete non-linear system in spherical component form is given by

$$(u_\lambda - Src\cos\phi)\frac{\partial h}{\partial \eta} + u_\phi \cos\phi \frac{\partial h}{\partial \phi} + h\left[\frac{\partial u_\lambda}{\partial \eta} + \cos\phi \frac{\partial u_\phi}{\partial \phi} - u_\phi \sin\phi\right] = 0, \tag{5}$$

$$(u_\lambda - Src\cos\phi)\frac{\partial u_\lambda}{\partial \eta} + u_\phi \cos\phi \frac{\partial u_\lambda}{\partial \phi} - \left(\frac{\cos\phi}{Ro} + u_\lambda\right)u_\phi \sin\phi + \frac{1}{Fr^2}\frac{\partial h}{\partial \eta} = 0, \tag{6}$$

$$(u_\lambda - Src\cos\phi)\frac{\partial u_\phi}{\partial \eta} + u_\phi \cos\phi \frac{\partial u_\phi}{\partial \phi} + \left(\frac{\cos\phi}{Ro} + u_\lambda\right)u_\lambda \sin\phi + \frac{\cos\phi}{Fr^2}\frac{\partial h}{\partial \phi} = 0, \tag{7}$$

where all field variables are now non-dimensional and will remain so for the rest of the paper. The three dimensionless numbers Sr, Ro and Fr are the familiar flow regime parameters from fluid dynamics and are given as

$$Sr = \frac{ac_{\text{ref}}}{v_{\text{ref}}} \quad \text{Strouhal number},$$

$$Ro = \frac{v_{\text{ref}}}{2\Omega a} \quad \text{Rossby number},$$

$$Fr = \frac{v_{\text{ref}}}{\sqrt{gh_{\text{ref}}}} \quad \text{Froude number}.$$

Eqs. (5)–(7) constitute the non-dimensional form of the shallow water equations that will be used as the basis of the dynamics in this paper.

2.2. Volume specification

In addition to the mass Eq. (5) and the two momentum equation components (6) and (7), it is also necessary to specify the total mass of the atmosphere. As this is an incompressible theory, this condition is equivalent to imposing the total volume V_{b} of the atmosphere. We now prescribe that there are exactly κ wavelengths in longitude around each latitude circle. The desired volume V of the atmosphere is now specified by integrating the region contained between the radial surfaces $r = a$ and $r = a + h(\eta, \phi)$ in a spherical coordinate system. Thus, we have

$$V = \int_0^{2\pi}\int_{-\pi/2}^{\pi/2}\int_a^{a+h(\eta,\phi)} r^2 \cos\phi \,\mathrm{d}r\,\mathrm{d}\phi\,\mathrm{d}\eta$$

which, after taking symmetry into account, may be simplified at once to give

$$V = \frac{4\kappa}{3}\int_0^{\pi/\kappa}\int_0^{\pi/2}\left[h^3 + 3\hat{a}^2 h + 3\hat{a}h^2\right]\cos\phi\,\mathrm{d}\phi\,\mathrm{d}\eta. \tag{8}$$

Here, $\hat{a}$ is the dimensionless form of the sphere's radius, scaled relative to h_{ref} (i.e., $\hat{a} = a/h_{\text{ref}}$). The volume specification condition is now written in the form

$$1 - \frac{V}{V_{\text{b}}} = 0. \tag{9}$$

The complete specification of a non-linear progressive Rossby wave in this model consists of solving (5)–(9) subject to some condition defining the amplitude of the wave. The particular form of the amplitude forcing will be discussed in Section 4.

3. Linearized theory – small amplitude waves

3.1. Linearization

In this section we present a linearized solution for the progressive wavespeed, based on small amplitude perturbations of a base eastward flow field. This is of interest in its own right, and will also guide the numerical solution of the full non-linear problem to be discussed in Section 4. Although the literature contains linearizations of the shallow water equations about quite general base flow representations (see, for example, Kasahara [22]), we will restrict our discussion to a specific type of base flow. Following the work of Haurwitz [4] we introduce a zonal flow in the form of a super rotation that only depends on latitude ϕ. Putting $u_\lambda = u_{\lambda z} = \omega \cos\phi$ and $u_\phi = u_{\phi z} = 0$ into (5)–(7) yields a differential equation for the zonal free surface height which is easily integrated to give

$$h_z = h_o + \frac{\omega Fr^2}{2}\left(\frac{1}{Ro} + \omega\right)\cos^2\phi, \tag{10}$$

where h_o is the dimensionless polar free surface height, ω is the dimensionless angular speed of the base zonal flow, and the additional subscript z denotes field variables belonging to the zonal flow structure.

We now assume that the flow may be regarded as a small $O(\epsilon)$ perturbation of the base zonal flow state, so that the velocity components and free surface height may be written in the form

$$u_\lambda(\eta,\phi) = u_{\lambda z} + \epsilon u_{\lambda 1}(\eta,\phi) + O(\epsilon^2), \tag{11}$$

$$u_\phi(\eta,\phi) = 0 + \epsilon u_{\phi 1}(\eta,\phi) + O(\epsilon^2), \tag{12}$$

$$h(\eta,\phi) = h_z + \epsilon h_1(\eta,\phi) + O(\epsilon^2). \tag{13}$$

Here ϵ can be thought of as a small parameter representing Rossby wave amplitude. Eqs. (11)–(13) are substituted into (5)–(7) and the set of equations are taken to $O(\epsilon)$, following well-known techniques in perturbation theory (see, for example, Van Dyke [23]). The solution of the resulting system is facilitated by noting that we may write each of the $O(\epsilon)$ perturbation terms as the product of a single Fourier mode in η with some function of ϕ. Thus we define

$$u_{\lambda 1}(\eta,\phi) = \cos(\kappa\eta)\Lambda(\phi), \tag{14}$$

$$u_{\phi 1}(\eta,\phi) = \sin(\kappa\eta)\Phi(\phi), \tag{15}$$

$$h_1(\eta,\phi) = \cos(\kappa\eta)\mathscr{H}(\phi), \tag{16}$$

where the parity of the Fourier basis in η in each term is chosen to preserve the parity of each of the dynamical Eqs. (5)–(7). Also note that the parameter κ, defined previously, has been introduced as a way of specifying the longitudinal wavenumber. This is a natural addition to the model since intuitively we would expect that the wavespeed c will depend on the number of equally spaced wavelengths around a latitude circle. By defining the $O(\epsilon)$ terms according to (14)–(16) we remove the η dependence entirely from the partial differential equations, transforming them into a set of ordinary differential and algebraic equations given by

$$-\kappa(\omega - Src)\cos\phi\mathscr{H}(\phi) + \Phi(\phi)\cos\phi\frac{dh_z}{d\phi} + h_z\left[-\kappa\Lambda(\phi) + \cos\phi\frac{d\Phi(\phi)}{d\phi} - \Phi(\phi)\sin\phi\right] = 0, \tag{17}$$

$$-\kappa(\omega - Src)cos\phi\Lambda(\phi) - \left(\frac{1}{Ro} + 2\omega\right)\Phi(\phi)\sin\phi\cos\phi - \frac{\kappa}{Fr^2}\mathscr{H}(\phi) = 0, \tag{18}$$

$$\kappa(\omega - Src)\Phi(\phi) + \left(\frac{1}{Ro} + 2\omega\right)\Lambda(\phi)\sin\phi + \frac{1}{Fr^2}\frac{d\mathscr{H}(\phi)}{d\phi} = 0. \tag{19}$$

3.2. Numerical solution approach

Solutions of (17)–(19) are sought in the form of truncated Fourier series with specific symmetry conditions. We restrict the set of possible solutions to those that have u_λ and h symmetric and u_ϕ anti-symmetric with respect to the equator ($\phi = 0$). Additionally we require that u_λ and u_ϕ are zero at the poles, while h needs to be constant at the poles ($\phi = \pm\pi/2$). An instance of functions that fulfil these prescribed conditions can be given by

$$\Lambda(\phi) = \sum_{n=1}^{N} P_{\kappa,n} \cos((2n-1)\phi), \tag{20}$$

$$\Phi(\phi) = \sum_{n=1}^{N} Q_{\kappa,n} \sin(2n\phi), \tag{21}$$

$$\mathscr{H}(\phi) = \sum_{n=1}^{N} H_{\kappa,n}(-1)^n[\cos(2n\phi) + \cos(2(n-1)\phi)], \tag{22}$$

where $P_{\kappa,n}$, $Q_{\kappa,n}$ and $H_{\kappa,n}$ are the series coefficients, subscript κ on each coefficient denotes the longitudinal wavenumber, and N is a positive integer truncation level. Note that in this analysis the meridional velocity is constrained to vanish at the poles for all positive values of κ, hence $\kappa = 1$ will not be considered in this manuscript since this case corresponds to flow over the poles and the above basis set would not be sufficient to describe these motions. The particular form of (22) involves basis recombination, and requires further explanation. Observe first that the free-surface height $h(\eta,\phi)$ in (13) is only required to be constant at the poles, with height h_o given in (10). Thus $\mathscr{H}(\phi) = 0$ at the poles. However, symmetry requires $\mathscr{H}(\phi)$ to be even, so that a Fourier series involving $\cos(2n\phi)$ terms is needed, and these attain the values ± 1 at the poles. Therefore, in order to make $\mathscr{H}(\phi)$ zero at $\phi = \pm\pi/2$, the rearrangement shown in (22) is necessary.

A standard Galerkin method is now used to determine the wavespeed c and associated coefficients $P_{\kappa,n}$, $Q_{\kappa,n}$ and $H_{\kappa,n}$. Series (20)–(22) are substituted into each of (17)–(19) and the resulting equations are multiplied by suitable base expansion functions, integrated over $-\pi/2 \leqslant \phi \leqslant \pi/2$ and equated to zero. Specifically, (17) is multiplied by $\cos((2j-1)\phi)$ for $j = 1,2,\ldots,N$, (18) is multiplied by $\cos(2j\phi)$ for $j = 0,1,\ldots,N-1$, and (19) is multiplied by $\sin(2j\phi)$ for $j = 1,2,\ldots,N$. The well-known orthogonality properties of trigonometric functions then lead to a matrix system of $3N$ equations. The full set of equations is too lengthy to give here, but significantly it may be expressed in the generalized eigenvalue form

$$A\boldsymbol{x} = cB\boldsymbol{x}, \tag{23}$$

where A and B are constant matrices corresponding to the left and right-hand sides of each of the algebraic equations obtained from orthogonality. The eigenvalue c is precisely the wavespeed for the progressive Rossby wave, and vector $\boldsymbol{x}$ is the eigenvector of unknown linearized coefficients, which is defined as

$$\boldsymbol{x} = [H_{\kappa,1},\ldots,H_{\kappa,N},P_{\kappa,1},\ldots,P_{\kappa,N},Q_{\kappa,1},\ldots,Q_{\kappa,N}]^{\mathrm{T}}. \tag{24}$$

We note that the general structure of both A and B is that of banded diagonal matrices with A also containing banded sub and super-diagonal components. In particular we note that diagonal matrix B consists of non-zero elements along the main diagonal and thus will be invertible, implying that it will always be possible to find solutions of the generalized eigensystem, provided $B^{-1}A$ is non-singular.

3.3. Model parameters

We now specify the particular values for the dimensionless parameters in the model. Although this analysis is not specific to a given sphere size or mass it seems reasonable to use parameters that closely approximate those of the Earth so that direct comparison can be made between the present model and other published results. With this in mind we adopt the following values for the sphere specific parameters:

$$a = 6.37122 \times 10^6 \text{ m}, \tag{25}$$

$$\Omega = \frac{2\pi}{24 \times 3600} \approx 7.272 \times 10^{-5} \text{ s}^{-1}, \tag{26}$$

$$g = 9.80616 \text{ m s}^{-2}. \tag{27}$$

Additionally we define each characteristic reference scale as

$$v_{\text{ref}} = 40 \text{ m s}^{-1}, \tag{28}$$

$$h_{\text{ref}} = 8.0 \times 10^3 \text{ m}, \tag{29}$$

$$c_{\text{ref}} = \frac{\Omega}{30} \approx 2.4241 \times 10^{-6} \text{ s}^{-1}, \tag{30}$$

so that the Strouhal, Froude and Rossby numbers are given by

$$Sr \approx 3.8611 \times 10^{-1}, \tag{31}$$

$$Fr \approx 1.4281 \times 10^{-1}, \tag{32}$$

$$Ro \approx 4.3166 \times 10^{-2}. \tag{33}$$

The small value of Ro is in agreement with the definition of large scale flow (see, e.g. Pedlosky [24]) so that we can expect the Earth's rotation to be an influential factor determining the nature of any calculated solution. This is precisely the kind of behaviour we seek, since we require flows in which the dominant driving force sustaining any initial perturbation is highly dependent on the large scale nature of the flow, as first demonstrated by Rossby [1].

For the dimensionless zonal flow parameters we choose values that are consistent with those documented in the test set of Williamson et al. [7]. The equivalent non-dimensional values for h_o and ω are $h_o = 1$ and $\omega = 1.25$. The particular value of ω is obtained by noting that Williamson et al. use a dimensional value for ω of 7.848×10^{-6} s^{-1}, a value first introduced by Phillips [8]. In order to convert this to a dimensionless number it is necessary to multiply by the radius of the Earth and divide by the reference velocity scale so that

$$\omega = \frac{7.848 \times 10^{-6} a}{v_{\text{ref}}} \approx 1.25. \tag{34}$$

Although (34) is only a single value of the dimensionless zonal flow angular speed, the analysis presented here permits a wide variety of values for ω, anticipating the strong dependence of the non-linear solution on ω to be discussed in Section 5.

It is also necessary to specify a base volume V_b for the system, to be used in the volume specification Eq. (9). For this study the value for V_b was chosen to be the total volume contained between the surface of the sphere and the free surface shape defined by the zonal flow with parameters $h_o = 1$ and $\omega = 1.25$. Thus the base volume is simply the total volume of the atmosphere corresponding to purely zonal flow with parameters equivalent to those used in Williamson et al. [7]. Since the linearized waves are effectively perturbations of the zonal flow, we need only match the volumes for each underlying zonal flow state because in the limit as $\epsilon \to 0$ the flow will reduce to this form.

The zonal flow is specified uniquely by the two parameters h_o and ω; hence the volume matching condition in the linearized case is equivalent to fixing ω and calculating the new polar height h_o that satisfies (9). This reduces to solving a cubic equation for h_o each time a new value of ω is specified, for the linearized theory. For the present purposes, the formula for the one real root of a cubic equation was used to solve for h_o (see, e.g. Abramowitz and Stegun [25]). Note that this implies an upper limit on the zonal flow angular speed, since the polar height h_o must decrease as the super-rotation rate increases, when volume remains fixed. An upper bound is therefore required for ω, to prevent h_o from becoming negative.

The solution of the generalized eigenvalue problem was achieved by implementing a MATLAB script that assembled the left and right hand side matrices and then solved the resulting system by using the inbuilt routine **`eig(A,B)`** to find the eigenvalues and corresponding eigenvectors. All computations were performed on an AMD Athlon(tm) XP 1800+ processor clocked at 1.54 GHz with 512 MB of physical memory. Various truncation levels were chosen to check convergence of the algorithm and in all cases rapid convergence was

observed for increasing N. Typically a truncation value of $N = 10$ was all that was required to establish the solution to 4 or 5 significant figures, when compared to higher truncation level solutions, and a truncation level of $N = 100$ could almost be deemed excessive if not for the very small computational times involved; approximately 3 s was required to compute all 300 eigenvalue–eigenvector pairs when $N = 100$.

4. Non-linear theory – large amplitude waves

4.1. Numerical solution method

Solutions of the fully non-linear equations given in (5)–(7) are sought using Fourier series with similar symmetry conditions imposed on the field variables as in Section 3.2. Additionally, it is no longer possible to use the constant of integration h_o as a zonal flow parameter because h_o effectively controls the free surface height at the poles, and in the non-linear model there is no way of knowing what this height will be prior to a computation. Instead, the polar height becomes an output of the model and is determined by finding $h(\eta,\phi)$ that solves (9) for a given value of V_b.

Taking symmetry and polar no-flow conditions into account, the series for the present unsteady progressive Rossby waves, using longitudinal truncation M and latitudinal truncation N, can be given by:

$$u_\lambda(\eta,\phi) = \omega\cos\phi + \sum_{m=1}^{M}\sum_{n=1}^{N} P_{m,n}\cos(\kappa m\eta)\cos((2n-1)\phi), \tag{35}$$

$$u_\phi(\eta,\phi) = \sum_{m=1}^{M}\sum_{n=1}^{N} Q_{m,n}\sin(\kappa m\eta)\sin(2n\phi), \tag{36}$$

$$h(\eta,\phi) = \sum_{n=0}^{N} H_{0,n}\cos(2n\phi) + \sum_{m=1}^{M-1}\sum_{n=1}^{N} H_{m,n}\cos(\kappa m\eta)(-1)^n[\cos(2n\phi)+\cos(2(n-1)\phi)]. \tag{37}$$

Here, (37) again uses basis recombination to satisfy conditions that the free surface height be an even function and constant at the poles. The series (35) for u_λ now contains the primary zonal flow velocity component. Instead of specifying the polar free surface height we replace h_o with the single summation term in (37) to allow the polar height to be determined from the output of the model, as discussed previously. Observe also that the surface elevation $h(\eta,\phi)$ in Eq. (37) is the only expression for which it is appropriate to include the $m = 0$ wavenumber mode. This is because of the need to specify the super-rotation term $\omega\cos\phi$ uniquely in Eq. (35) (to avoid an over-determined system), and to enforce the odd symmetry in Eq. (36). As a result, one fewer azimuthal mode m can be determined numerically in Eq. (37) if each series is to have exactly $M \times N$ unknown coefficients.

To close the system of equations it is necessary to specify either the amplitude, denoted $\mathscr{A}$ and defined later in Section 4.2, in terms of one of the unknown coefficients, or the wavespeed c. To this end $H_{1,1}$ in the series for $h(\eta,\phi)$, or the wavespeed c, is fixed prior to computation, thus removing one of the unknowns from the problem. The majority of computations were performed by specifying $H_{1,1}$, and the second technique of specifying c was reserved for cases where two or more solutions were possible with the same amplitude.

The general solution process consists of finding the set of coefficients $H_{m,n}$, $P_{m,n}$, $Q_{m,n}$ and wavespeed c that make the series (35)–(37) a solution of the dynamical system described by (5)–(9). The technique chosen to accomplish this task for the current work is the pseudospectral technique of collocation in which we require the residuals, obtained by substituting the series into the governing equations, to be zero at every point on a mesh constructed from a finite number of points in the flow field (see, e.g. Duran [26]).

For the collocation points in ϕ we restrict computation to the Northern hemisphere since the solution has specific symmetry relative to the equator. In addition, strictly internal points from the domain are chosen, since the specific choice of the basis functions for each series imposes boundary conditions at both $\phi = 0$ and $\phi = \pm\pi/2$. Defining

$$\Delta\phi = \frac{\pi}{2(N+1)} \tag{38}$$

to be the inter-grid point distance in the ϕ direction, the N equally-spaced ϕ-grid points are

$$\phi_i = i\Delta\phi, \quad \text{for } i = 1, 2, \ldots, N. \tag{39}$$

The collocation points in η can be obtained in a similar manner; however, since we have stipulated a dependence on the wavenumber κ, we are only free to choose collocation points from $\eta \in [0, \pi/\kappa)$, to avoid linearly dependent rows in the residual vector and resulting Jacobian matrix. This also accounts for the fact that the Rossby wave is symmetric about its mid-line $\eta = \pi/\kappa$. Defining

$$\Delta\eta = \frac{\pi}{M\kappa} \tag{40}$$

to be the inter-grid point distance in the η direction, the M equally spaced η-grid points are

$$\eta_j = (j-1)\Delta\eta, \quad \text{for } j = 1, 2, \ldots, M. \tag{41}$$

The set of points taken from all possible (η_j, ϕ_i) pairs constitutes the collocation mesh. Note that we have imposed upper limits on i and j in Eqs. (39) and (41) so that the number of grid points in the collocation mesh is equal to the number of unknown coefficients, thus establishing a connection between the collocation mesh and the series coefficients.

Evaluating each of the three governing Eqs. (5)–(7) at each of the collocation mesh points and computing the volume specification condition (9) yields a vector of residuals, denoted $\vec{E}(\vec{x})$, of length $3MN + 1$, where $\vec{x}$ is a vector comprised of the wavespeed (if it is not the forcing term) and the unknown coefficients. A damped Newton–Raphson method (see, e.g. Press et al. [27]) is then used to solve the resulting algebraic system, which has the general form

$$\vec{E}(\vec{x}) = \vec{0}. \tag{42}$$

Specifically, an initial guess at the vector of unknowns $\vec{x}^{(k)}$ is defined, where the superscript k denotes the current iterative step. An updating direction $\vec{\delta x}^{(k)}$ is then computed as the solution of the linear system

$$J^{(k)}\vec{\delta x}^{(k)} = -\vec{E}(\vec{x}^{(k)}), \tag{43}$$

where $J^{(k)}$ is the Jacobian matrix of partial derivatives of the components of the residual vector $\vec{E}(\vec{x}^{(k)})$. Once the updating direction is determined, the solution vector is corrected using

$$\vec{x}^{(k+1)} = \vec{x}^{(k)} + \vec{\delta x}^{(k)} \tag{44}$$

and the process is then repeated, starting from the new point $\vec{x}^{(k+1)}$, until Eq. (42) is satisfied to within a prescribed error tolerance. The Jacobian matrix, which is required to compute the updating vector in (43), is calculated analytically in this study, since the Jacobian elements are, in general, easily determined. Additionally, the magnitude of the total residual error, which is used in assessing the convergence of a solution, is computed using the L^1 norm (the sum of absolute values).

The starting guess at the set of unknowns $\vec{x}$ in the Newton–Raphson method is initially determined from the corresponding linearized solution for the same values of κ, ω and V, given in Section 3. Once a small amplitude non-linear solution has been determined, it is then used as the basis for the next solution to be computed but with an increased value, as a small percentage of the previous solution value, of either c or $H_{1,1}$, depending on the type of forcing. This bootstrapping procedure forms the basis of mapping the wavespeed versus amplitude relationship incrementally.

Computational efficiency is achieved by caching each of the basis functions and their derivatives with respect to η and ϕ at each of the collocation mesh points; this approach reduces the computational overhead incurred by repeated function calls to the trigonometric functions. The integral appearing in (8) is evaluated using numerical quadrature. The particular algorithm used is that of adaptive Lobatto quadrature, with Kronrod extension of the Gauss–Lobatto formula, as detailed in Gander and Gautschi [28]. The majority of computations were performed on two separate computers, the first being an AMD Athlon(tm) XP 1800+ processor clocked at 1.54 GHz with 512 MB of physical memory, the second being an Athlon(tm) XP 2800+ processor clocked at 2.08 GHz with 1 GB of dual channel physical memory.

4.2. Amplitude measurement

In order to investigate the relationship between the progressive Rossby wavespeed and amplitude, we require a means of defining the amplitude $\mathscr{A}$ of a particular Rossby wave. For a simple periodic wave, the amplitude can be defined as the maximum deviation from the mean position to an extreme point. The problem of measuring Rossby wave amplitude horizontally on a sphere is somewhat more complicated and arbitrary, however. Due to the multitude of wave shapes that are possible, there are an infinite number of mean states about which we can measure wave deviation. We must therefore decide on which one is appropriate to use. Because Rossby wave activity is predominantly associated with the mid-latitude regions, and also because $\phi = \pm\pi/4$ represents the mid-point between the equator and either pole, we choose the mean reference level as the latitude circle located 45° from the equator in either hemisphere.

In this context, progressive Rossby waves are perturbations from a base zonal westerly flow, for which the height contours of (10) would simply be circles of constant ϕ. The unperturbed free-surface height contours at $\phi = \pm\pi/4$ are taken here as the base level, against which Rossby wave amplitudes are measured.

Observe that the amplitude will not be the same in both the equator-ward and pole-ward directions, and the difference between the two will increase as the overall wave amplitude grows. Because of the geometry of the sphere it is possible for a Rossby wave to extend further towards the equator than towards the pole where the lines of longitude converge. Thus to record $\mathscr{A}$ effectively we need to measure both the equator-ward and pole-ward deflections, which we denote $\mathscr{A}_e$ and $\mathscr{A}_p$, respectively. Associated with these separate but related amplitudes we define a simple averaged amplitude, the mean of the two values, to be

$$\mathscr{A}_{ave} = \frac{\mathscr{A}_e + \mathscr{A}_p}{2}. \tag{45}$$

To actually compute these amplitudes it was necessary to first solve for the series coefficients and then use MATLAB to generate a high density map of the free surface contours. The deformed contour corresponding to the originally unperturbed $\phi = \pi/4$ contour level was then located and used to determine the maximum equatorial and poleward deviations of the contour about the $\phi = \pi/4$ latitude circle. A MATLAB script was written to specifically accomplish this task.

When we present specific results in Section 5.2 we will plot the wave speed c versus each of the above defined amplitudes, namely $\mathscr{A}_e$, $\mathscr{A}_p$ and $\mathscr{A}_{ave}$. It is important to emphasize that these definitions of amplitude measurement are somewhat arbitrary, although they are a useful way of quantifying transverse amplitudes on a spherical surface.

4.3. Model parameters

The parameters and constants for the model are again chosen to approximate those of the Earth, as in Section 3.3. Specifically, the parameters a, Ω and g, as well as the three reference scales v_{ref}, h_{ref} and c_{ref} are given by (25)–(30), respectively. For the dimensionless zonal flow parameter ω we use two specific values. In the linearized model it is possible to specify a broad range of ω values with little overhead incurred in terms of time taken to perform numerical calculations. Unfortunately, in the non-linear model, we are no longer able to investigate the solution dependency on ω without incurring a significant increase in the computation time. This is because at each value of ω chosen a complete solution curve for the c versus $\mathscr{A}$ relationship must be computed, which involves many possible values of the wavespeed, rather than the single value computed in the linearized model. On average, to compute a complete solution curve at a reasonable truncation level for a fixed value of ω, many weeks of computational time was required for programs executing on the previously documented hardware specifications in Section 4.1.

For this reason it was decided to focus attention on two specific values of the parameter ω. The first value is consistent with the angular speed ω used in the test set proposed by Williamson et al. [7]. The second value, chosen to be 80% of the first value, provides a slower and perhaps physically more realistic value for the super rotation rate. In dimensionless form the two values are given by

$$\omega_1 = 1.25, \tag{46}$$

$$\omega_2 = 1.0. \tag{47}$$

It is also necessary to specify a base volume V_b for the system, to be used in the volume specification equation given by (9). For this study the base volume is simply the total volume of the atmosphere corresponding to purely zonal flow with parameters equivalent to those used in Williamson et al. [7], as in the linearized solution approach of Section 3.3.

5. Presentation of results

5.1. Linearized solution results

Although the linearized eigensystem (23) has $3N$ eigenvalue–eigenvector pairs for integer truncation N, in this study we are only concerned with the fundamental solution of the system. Physically, this represents the longest wavelength linearized solution, rather than higher-order harmonics. To provide evidence supporting the accuracy of the linearized solutions computed, it is useful to make a comparison between these solutions and the equivalent corresponding Rossby–Haurwitz solutions. It is useful to do this because, although the mathematical descriptions for each model differ, they both model the same fundamental process and both models assume a base zonal super rotation from which waves are perturbed about. To make the comparison we make use of the wavespeed formula derived by Haurwitz [4]. The particular formula is given by

$$c = \frac{\kappa(3+\kappa)\omega - 2\Omega}{(1+\kappa)(2+\kappa)} \tag{48}$$

which has been rewritten to reflect the naming conventions and variable names used in this work. Note that this equation clearly shows a linear relationship between c and ω. In addition, the Haurwitz model has no provision for fixing the volume V_b of the atmosphere, since it does not assume the presence of a free surface for the atmosphere. Consequently, differences are to be expected between that model and the work presented here.

To compare the two solution types we consider the fundamental eigenvalues for $\kappa = 3$, 4 and 5 with the equivalent Rossby–Haurwitz solutions over a range of allowable ω values. Fig. 1 shows the results of this comparison, with the solid lines representing the equivalent Rossby–Haurwitz solution for $\kappa = 3$–5 from bottom to top, respectively. Dimensionless units are assumed in this figure, corresponding to parameters appropriate to the Earth, as explained in Section 3.3. The original dimensional angular speeds and wavespeeds may therefore

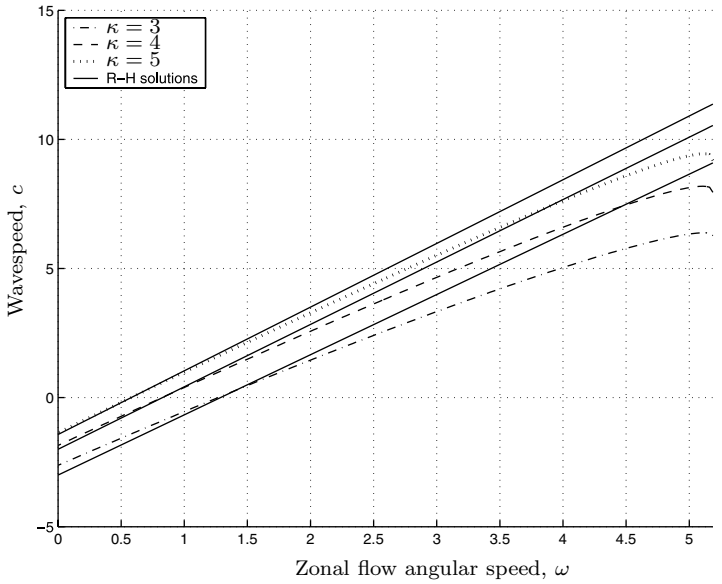

Fig. 1. Comparison of linearized and Rossby–Haurwitz solutions (solid lines) for $\kappa = 3$, 4 and 5 and $N = 100$. The linearized results are shown with dot-dashed, dashed and dotted lines, for $\kappa = 3$, 4 and 5, respectively.

be obtained from Fig. 1 simply by multiplying values on the horizontal and vertical axes by the quantities $v_{\text{ref}}/a = 6.278 \times 10^{-6}$ rad s^{-1} and $c_{\text{ref}} = 2.4241 \times 10^{-6}$ s^{-1}, respectively.

In general one can conclude that the two models are in good broad agreement, especially so for values of ω in the range $0 < \omega < 2$ where the effect of the volume matching is minimal. Note that for each of $\kappa = 3$, 4 and 5 there is a value of ω for which $c = 0$, so that the linearized Rossby wave structure remains stationary relative to the Earth's surface. For values of ω below this critical value we have wave motion towards the West whereas for values higher we have Eastward wave motion, allowing for a wide variety of atmospheric configurations. Note that the bending over of the linearized solutions for large values of ω is a consequence of the fact that the height at the poles, h_{o}, is changing to conserve the total volume, as previously discussed.

It is also useful to examine the resulting free surface contours produced by both models. In order to match the height contour levels it necessary to specify some equivalent value of the wave amplitude ϵ. To make comparison possible we choose to match the two height fields at $(\eta, \phi) = (0, \pi/4)$ which represents a reasonable mid-point level in each contour set. It is interesting to note that despite the fact that Haurwitz did not use a free surface formulation, a resulting height field may be calculated via an analysis of the pressure field by noting that pressure is converted into an equivalent free surface height under hydrostatic assumptions, as developed by Phillips [8].

Figs. 2 and 3 provide a solution comparison both qualitatively, through a visual comparison, and quantitatively, through the specific contour levels of each height field. The latitudinal circle at $\phi = \pi/4$ is indicated to show where the match takes place. The dimensional heights may be recovered from the contour values in the figures simply by multiplying by $h_{\text{ref}} = 8.0 \times 10^3$ m. All contour plots were made using a polar stereographic projection of the Northern Hemisphere, described exhaustively by Snyder [29]. Of particular interest is the slight pinching of crests and troughs for the Rossby–Haurwitz wave structure that is not evident in the linearized solution. This in turn forces the lower heights, and hence pressures, near the poles to extend further towards the equator in the Rossby–Haurwitz solution. However, overall there is very close agreement between both solution types.

5.2. Non-linear solution results

5.2.1. Results for $\kappa = 4$, $\omega = 1.25$

Fig. 4 shows wavespeed c computed for $\kappa = 4$ and $\omega = 1.25$, for each of the three measures of amplitude $\mathscr{A}_{\text{e}}$, $\mathscr{A}_{\text{p}}$ and $\mathscr{A}_{\text{ave}}$ defined in Section 4.2. As indicated previously and in Section 3.3, dimensional wavespeeds can be recovered from this diagram simply by multiplying values on the vertical axis by the quantity $c_{\text{ref}} = 2.4241 \times 10^{-6}$ s^{-1}. The figure is comprised of a total of 100 separately computed solutions. The truncation levels are $M = 20$ and $N = 20$ so that each series has a total of 400 coefficients, with a total of 1201

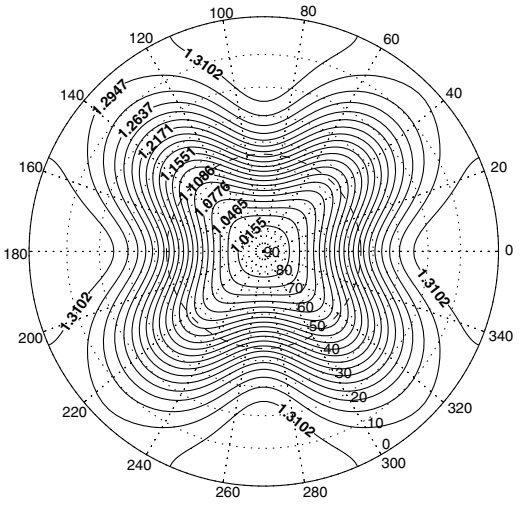

Fig. 2. Linearized free surface contours for $\kappa = 4$ with $N = 100$.

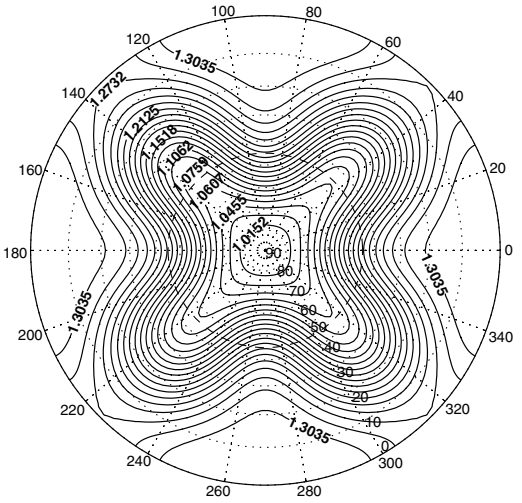

Fig. 3. Rossby–Haurwitz free surface contours for $\kappa = 4$.

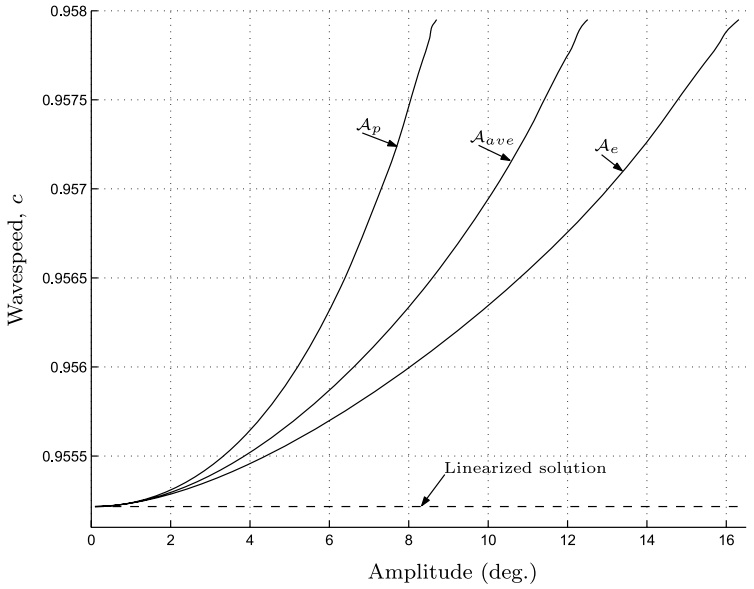

Fig. 4. Wavespeed versus amplitude relationship for $\kappa = 4$ and $\omega = 1.25$.

unknowns in the Newton's method algorithm (43). Results were initially computed at a lower truncation level of $M = N = 10$ to ascertain convergence of the numerical method. Once convergence of the solution was established, M and N were increased. The error tolerance on the L^1 norm of the residual vector was set at 10^{-12}, leading to average individual residual errors of the order of 10^{-15} or less, so that the governing equations were satisfied to the full accuracy possible on the computer. Solutions for the two truncation levels, $M = N = 10$ and $M = N = 20$, were compared and the resulting series coefficients were found to agree to at least 6 significant figures, providing evidence for the numerical convergence of the solutions calculated. In particular, bootstrapping was used to increase the truncation level beyond $M = N = 20$ for a random sample of points on the solution curve, and in all cases these higher resolution solutions were found to differ negligibly from those for $M = N = 20$, and, at least for small amplitude, from those of $M = N = 10$ as well.

The linearized solution is included and indicated with a dashed line in Fig. 4, showing that for small amplitude waves the wavespeeds computed from both the linearized and the fully non-linear theories are essentially equivalent. As the amplitude increases the wavespeed also increases, with the curve initially being tangential to

the linearized result for small $\mathscr{A}$ but diverging f[redacted] increasing more rapidly as $\mathscr{A}$ becomes larger. This behaviour is as expected b[redacted]ar wave calculations for gravitationally influenced incompressible fluids, n[redacted]rtz [31] and Cokelet [32]. These results, along with contributions from other [redacted]ummarized in the review article by Schwartz and Fenton [33].

As the amplitude continues to increase, t[redacted]dly until, ultimately, a limiting case is achieved numerically, where a slight c[redacted]ed. The physical explanation of this limiting solution is not clear from this ex[redacted], for example, that a sharp crest might be formed somewhere in the flow fie[redacted]ed water-wave case studied by Stokes and later by Schwartz. Alternatively, [redacted]tion is topologically limited, as found for gravity waves with surface tensio[redacted]ck [13], and Chen and Saffman [34]. However, an analysis of the polar ster[redacted]at this limiting wavespeed and amplitude combination, as shown in Fig. 5, [redacted]is present.

We suggest, however, that some type of n[redacted]ccurs, which is not accessible t[redacted] this numerical scheme because of the comple[redacted] implied sensitivity of Newto[redacted] method to the initial guess used. General e[redacted]t is presented in Section [redacted] Indeed, it is suspected that the limiting solut[redacted]s the largest amplitude [redacted] on one particular branch only, and that othe[redacted]ger amplitudes and w[redacted] Attempts to find such larger waves were mad[redacted]rticular the algorit[redacted] ged so that the wavespeed became the forci[redacted]k for faster pr[redacted] however, convergence of the residual vector [redacted]

5.2.2. Results for $\kappa = 4$, $\omega = 1.0$

The solution curves shown in Fig. 6[redacted]alues κ [redacted] consist of 143 separately converged so[redacted]t at M [redacted] mapped out using $M = N = 10$; little [redacted]ee[redacted] tolerance on the L^1 norm of the residu[redacted] of the order of 10^{-15} or less. Like the [redacted] small amplitude waves and as $\mathscr{A}$ incre[redacted] for $\omega = 1.25$, distinct discontinuous [redacted] branches, between which no numerica[redacted] vidual branches have been labelled in [redacted]re a[redacted] respectively.

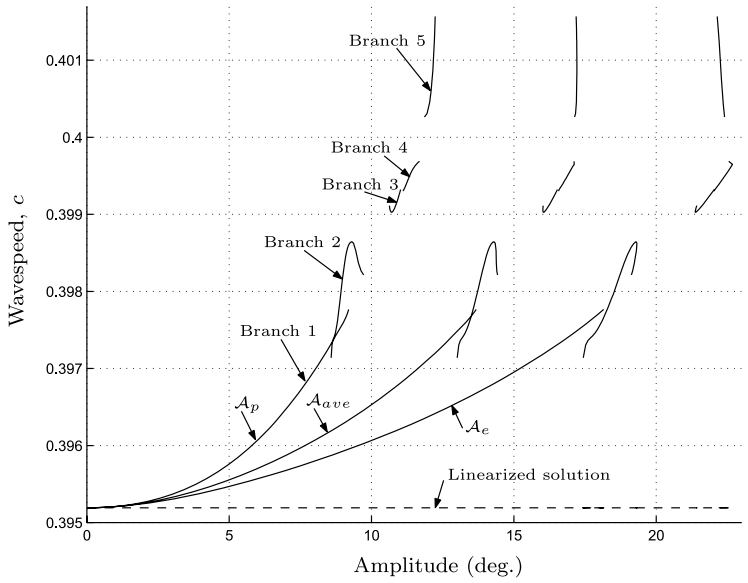

Fig. 6. Wavespeed versus amplitude relationship for $\kappa = 4$ and $\omega = 1.0$.

Discrete branching of the solution, as evidenced in the present results, is characteristic of non-linear resonance interaction in general, in which certain energy states of the system can be viewed as sympathetically exciting the underlying wave motion, undergoing energy exchange between waves of different wavelengths in the process. Non-linear resonance has been known to exist in complex non-linear wave propagation problems for some time now. In the context of gravity waves with surface tension Wilton [12] encountered key values of the capillary number at which resonance occurred. Schwartz and Vanden-Broeck [13], and Hogan [14–16], confirmed this behaviour in detail, by numerically solving the exact equations, and found that multiple simultaneous solution branches were possible. Forbes [17,18] also found resonant behaviour for surface waves of large amplitude beneath an elastic sheet.

To understand how the resonance is occurring in this particular example we can view the system as being forced by the parametrized amplitude through the Fourier coefficient $H_{1,1}$. As $H_{1,1}$ increases, $\mathscr{A}$ and c also increase until a point is reached where some of the Fourier modes in the series expansions are naturally excited by the forcing and can absorb energy via non-linear interactions. At this point resonance occurs, implying the coexistence of two or more solutions with commensurate frequency and wavenumber. Thus at resonance the Newton scheme has at least two solutions from which to choose and needs more information to make the choice. We also note that is possible that the current restriction of c real precludes the Newton method uncovering a complex conjugate pair of solutions brought about by the coalescence of frequencies. However, the method used is still able to expose fundamental resonances of the system where full time dependence would be necessary to discern the complete behaviour of the dynamical system.

The separate branches of the solution curve shown in Fig. 6 can be classified, at least partially, in terms of the general associated height field structure and corresponding velocity vector field along each solution curve segment. On branch 1 we conclude that at no point in the flow does the fluid move counter to the general direction of the overall wave propagation direction and additionally that the only stagnation points in the flow field are located at either of the two coordinate singularities, as expected. The free surface contours at the limiting upper value of branch 1 are shown in Fig. 7. It is observed that the general character of these contours is quite similar to those obtained with both the linearized model and Rossby–Haurwitz theory.

For solutions along branch 2, not much difference was observed between those along branch 1, with the general flow properties of the previous paragraph applying equally well here. It is also important to emphasize that the apparent intersection of branches 1 and 2 in the diagram is not a bifurcation point. Examination of the Fourier coefficients in the neighbourhood of the overlap shows distinctly different solution structure for each branch which fail to converge to a common set, despite the fact that the values of $\mathscr{A}$ and c for the

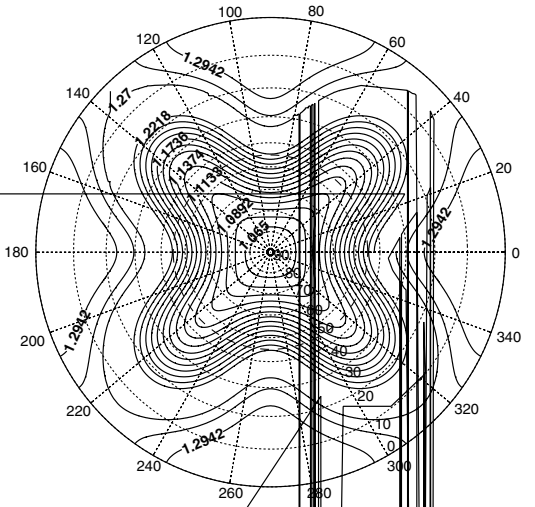

Fig. 7. Free surface contours at end of branch 1 for $\kappa = 4$, $\omega = 1.0$. The average amplitude is $\mathscr{A}_{\text{ave}} = 13.6732$ (°) and the wavespeed is $c = 0.3978$ (period of 75.41 days).

two branches coincide at this point. It would be possible to prove this with a simple analysis of the determinant of the Jacobian near the point of apparent intersection, as in Chen and Saffman [35]; however, the ease with which the Newton method iterates through this region seems to suggest that no further investigation is necessary with regard to the possible existence of a bifurcation. Additionally, the solution curve for the equatorial amplitude $\mathscr{A}_{\text{e}}$ does not contain the intersection, which confirms the presence of a resonance, instead of a simple bifurcation.

Solutions on branches 3 and above reveal richer structures in terms of more stagnation points in the flow field, reverse flow leading to localized circulation, and highly non-linear wave profiles. The main difference between the lower solution branches 1 and 2 and the upper solution branches 3, 4 and 5 can be expressed by examining the number of stagnation points in the flow field, disregarding the obvious polar stagnation points that all solutions must have by definition of the series expansions themselves. It is evident that for solutions on branches 3 and higher, all have stagnation points located symmetrically on the equator about the coordinate lines $\eta = 2n\pi/\kappa$, for $n = 0, 1, \ldots, \kappa - 1$. The exact position of these stagnation points was noted to change as the amplitude varied, although typically they were located quite close to the symmetry lines themselves. In between the two stagnation points the fluid was observed to flow counter to the general direction of the progressive wave movement. The height field was examined for small-scale localized high-pressure cells at these points of circulation, but none were found.

Fig. 8 shows a typical free surface contour plot for solutions along branches 3 and 4. The figure actually shows the contours at the limiting upper value of branch 4 and so represents the maximum allowable amplitude for waves on branch 4. It seems, from an analysis of the velocity fields and height contours, that the qualitative difference between waves on branches 3 and 4 is negligible. Nonetheless, a distinct gap was encountered when trying to establish the continuity of the solution between branches 3 and 4. Further investigation is needed to establish the key qualitative differences between these two branches, although this is both beyond the scope and computational capability of the present work.

Of particular note is the way in which low-level polar heights, and hence pressures, are seen to move equator-ward for solutions along these branches. It is suspected that the limiting factor for wavespeeds and amplitudes towards the upper end of branch 4 is directly related to the geometry of the low-level free surface contours which are not able to bend inwards any further without creating an isolated cut-off low-pressure system in the flow field. This statement is supported by the following analysis of branch 5 solutions.

The highly non-linear free surface height contours for the upper end of branch 5 are shown in Fig. 9. It is immediately evident that solutions along this branch have the distinguishing feature of cut-off low-pressure cells which are isolated from the general progressive wave structure. In addition to the already mentioned stagnation points in the flow field for waves on branches 3 and higher, more stagnation points are introduced for

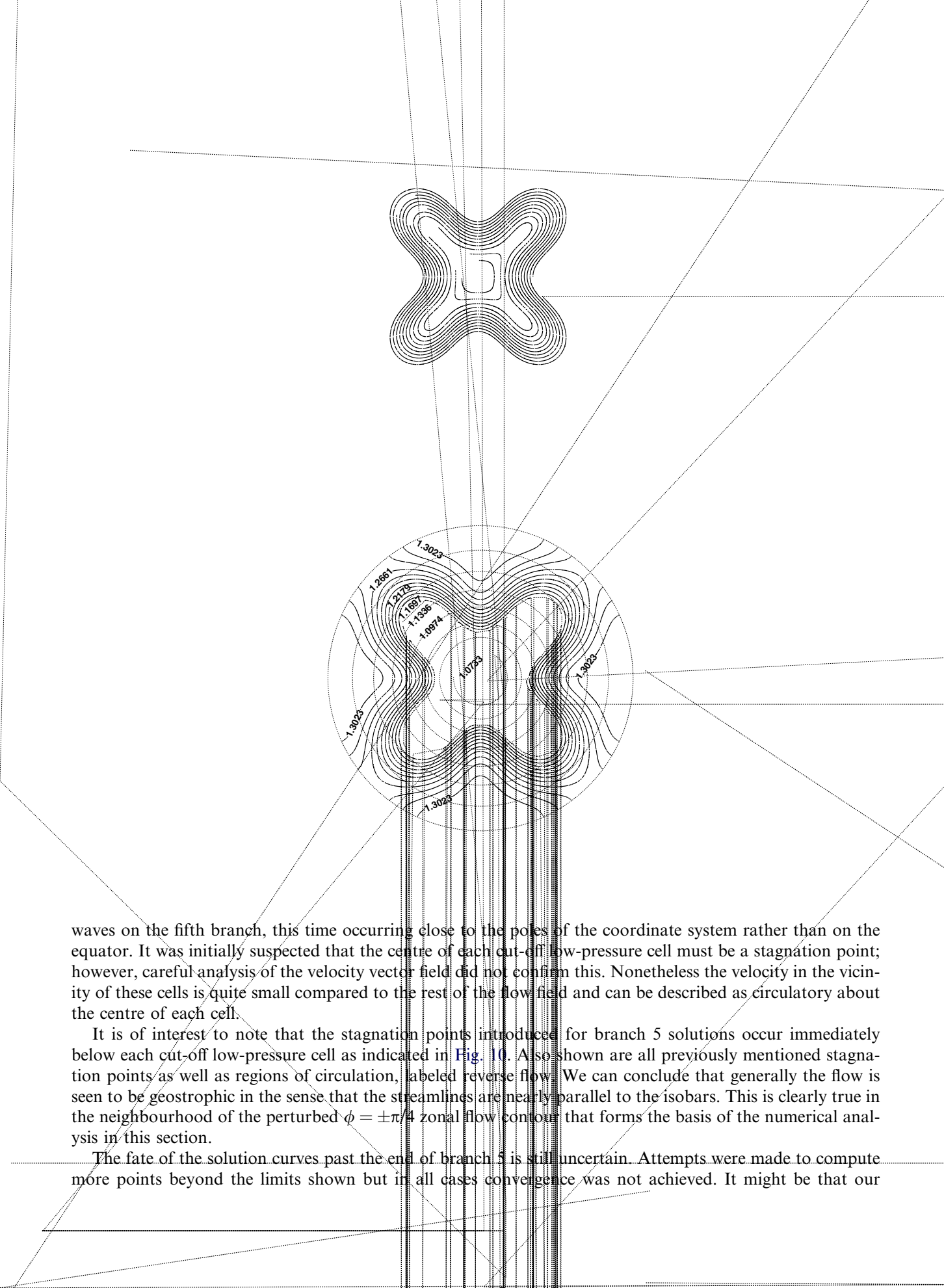

waves on the fifth branch, this time occurring close to the poles of the coordinate system rather than on the equator. It was initially suspected that the centre of each cut-off low-pressure cell must be a stagnation point; however, careful analysis of the velocity vector field did not confirm this. Nonetheless the velocity in the vicinity of these cells is quite small compared to the rest of the flow field and can be described as circulatory about the centre of each cell.

It is of interest to note that the stagnation points introduced for branch 5 solutions occur immediately below each cut-off low-pressure cell as indicated in Fig. 10. Also shown are all previously mentioned stagnation points as well as regions of circulation, labeled reverse flow. We can conclude that generally the flow is seen to be geostrophic in the sense that the streamlines are nearly parallel to the isobars. This is clearly true in the neighbourhood of the perturbed $\phi = \pm\pi/4$ zonal flow contour that forms the basis of the numerical analysis in this section.

The fate of the solution curves past the end of branch 5 is still uncertain. Attempts were made to compute more points beyond the limits shown but in all cases convergence was not achieved. It might be that our

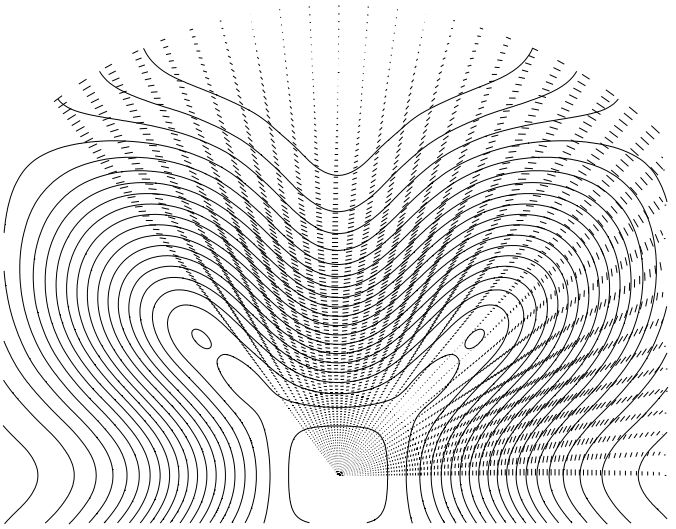

numerical method is not well suited to computing past points where the slope of the curve is nearly infinite, in which case improved techniques are required to investigate the behaviour past the limit shown. Alternatively this may be close to the maximum allowable amplitude of the system, imposed as a consequence of the finite size and geometry of the sphere.

5.2.3. Results for $\kappa = 5$, $\omega = 1.25$

It is of interest to study how the behaviour changes with an alternative value of the wave number κ. We now present results obtained with $\kappa = 5$, using the same pair of values ($\omega = 1.25$ and $\omega = 1.0$) for the dimensionless zonal flow super rotation; in this section we examine the case $\omega = 1.25$. Fig. 11 shows the computed

wave-speed versus amplitude relationship using a truncation of $M = N = 20$ for 203 individually converged solutions. The error tolerance on the L^1 norm of the residual vector was set at 10^{-12}, leading to average individual residual errors of the order of 10^{-15} or less.

The same general trend as for $\kappa = 4$ is encountered here for $\kappa = 5$, with the linearized solution being a good approximation to the non-linear solution for small $\mathscr{A}$ and the wavespeed becoming increasingly greater as the amplitude is increased. It appears that the use of $\kappa = 5$ introduces a new phenomenon in the form of a localized cubic structure located near $c \approx 1.5807$. It was initially suspected that this was in fact two distinct branches separated by a resonance; however, it was possible to compute continuously through this region, using a very small step size, without encountering any non-convergent solutions.

Therefore it seems that there are at least two explanations for this behaviour. The first is that there is in fact a resonance occurring near the point of inflexion, but existing on such a small scale that we were unable to detect in on any occasion. This does not seem very likely given the nature of the previous non-linear resonances observed for the case $\kappa = 4$, $\omega = 1.0$. The second explanation is that this is a feature of the dynamics and forcing, in which energy exchange between certain wavelengths is taking place in such a manner as to increase the overall amplitude while at the same time reducing the wave-speed. If so, this would represent a type of damped resonance, but careful analytical work, beyond the scope of this study, would be needed to identify the physical nature of the damping mechanism. Despite this localized reversal of the general trend of the graph, no obvious distinguishing features are visible when we examine the free surface contours and velocity vector field in the vicinity of this solution region. This fact seems to support the conjecture that separate resonance branches do not exist in this case, near $c = 1.5807$.

Two separate solution branches were found to exist towards the upper end of the curve when the limiting wavespeed–amplitude combination was approached. Because it is not entirely clear from the figure, it needs to be emphasized that the first branch terminates in the vicinity of $c \approx 1.5812$; thus the highest possible wavespeed indicated is at the right end of branch 2. It is again unlikely that the apparent intersection of the two branches is a sign of a simple bifurcation, for reasons outlined in the previous section.

For the left end of the second branch, numerical results have in fact been computed well beyond the termination point shown in the figure. However, it appears that they are of questionable value due to increasing numerical error along that branch and have therefore not been shown. The ultimate fate of this upper branch is not clear and may perhaps require alternative numerical techniques to reveal. In any event it is possible that this branch is physically unstable, the system preferring the lower wavespeed over the higher one, and so would generally not be observed in practice. It is even possible that a physical instability in this branch might produce a numerical instability, since the numerical iteration process may be equivalent to stepping forward in time (see, e.g. Ames [36]).

Typical free surface contours of the system are presented in Fig. 12, showing the nature of the solution at the end of branch 1. In contrast to the highly non-linear structures computed at the end of the curve for $\kappa = 4$ and $\omega = 1.0$, these contours demonstrate the significantly smaller maximum amplitude for which a convergent wavespeed was able to be calculated. In addition, no defining qualitative features of the velocity field were found that could be used to distinguish easily between the two solution branches. It is possible that more solution curves exist beyond those that are indicated; however, attempts to find such solutions were not successful.

5.2.4. Results for $\kappa = 5$, $\omega = 1.0$

For completeness we present results in this final section for $\kappa = 5$ and $\omega = 1.0$. Fig. 13 shows the computed solution curves obtained with the truncation level $M = N = 15$ for 100 individually converged solutions. The error tolerance on the L^1 norm of the residual vector was again set at 10^{-12}. The general features of this figure are less remarkable than those for the preceding set of results obtained with $\omega = 1.25$, although there is some evidence for a similar localized cubic structure, this time in the vicinity of $c = 0.99395$. The severity of this local cubic behaviour, however, is significantly less noticeable and does not substantially influence the general increase of c with $\mathscr{A}$. As in all previous solution curves presented, the results here agree well with the linearized value of the wavespeed for small values of the amplitude.

Typical free surface contours at the right end of the one and only computed branch are shown in Fig. 14. The waves shown are in general highly non-linear and it should be noted that the maximum pos-

sible amplitude obtained with this slower zonal super rotation speed is larger than that obtained with $\omega = 1.25$. No additional stagnation points in the flow field were observed, as in the previous case, and consequently all fluid flow was found to be in the same direction as the direction of propagation of the progressive wave.

It is again suspected that there are in fact more solution branches in addition to the one shown in Fig. 13. To support this statement we argue that the general nature of the flow field at the limiting computed value seems to be rather well behaved with no clearly identifiable limiting features. Unsuccessful attempts were made to bootstrap the limiting solutions to those on another higher branch; in all cases adequate convergence of the residual vector was not achieved.

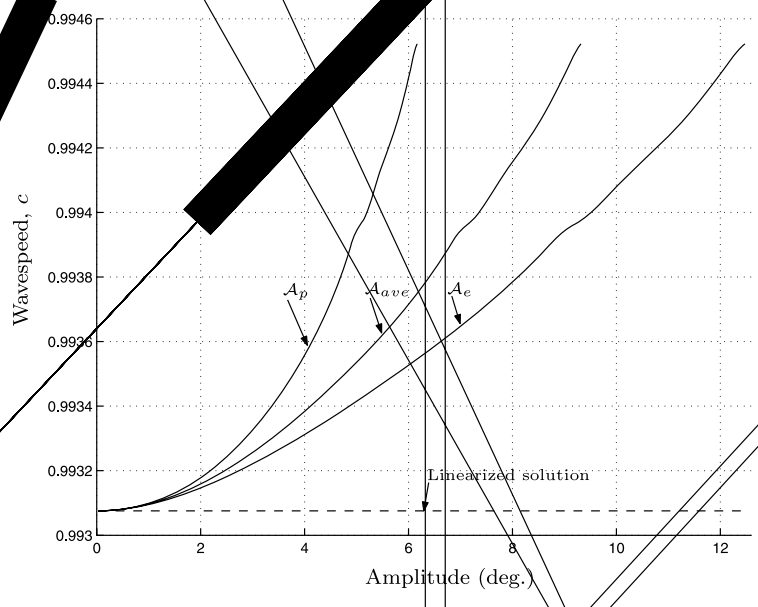

Fig. 13. Wavespeed versus amplitude for $\kappa = 5$ and $\omega = 1.0$

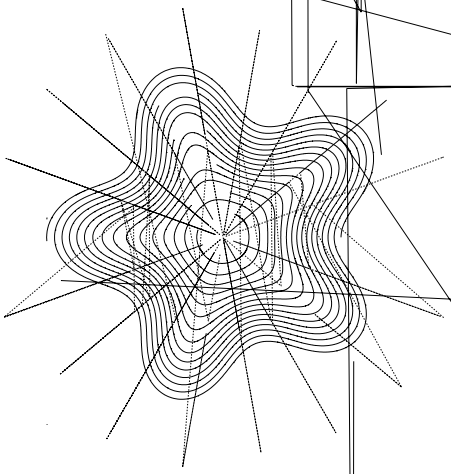

6. Discussion and conclusion

In this paper we have presented a detailed picture of how the effects of non-linearity influence the relationship existing between wavespeed and amplitude for progressive Rossby waves. The techniques utilized have uncovered feature-rich dynamical properties of progressive-wave solutions of the incompressible shallow atmosphere equations on a rotating sphere. In particular it was shown that non-linear resonance plays an important and dominant role for waves with large amplitudes. The effect of resonance was observed to separate solutions of the system into disjoint regions, with similar solutions lying on the same solution branch in wavespeed–amplitude space.

For slowly propagating progressive waves with longitudinal wavenumber $\kappa = 4$ and zonal flow angular speed $\omega = 1.0$, it was shown that if the amplitude forcing becomes large enough it is possible for the flow to develop localized low-pressure cells in the mid-latitude regions. These types of extreme amplitude solutions were accompanied by stagnation points in the flow field at locations other than the poles. In general it was observed that for these highly non-linear waveforms the lower polar free-surface heights, and hence pressures, and also the higher equatorial free-surface elevations, tended to be grossly distorted so that it was common for contours originating near the equator or pole to be deformed towards regions well in excess of the mid-latitudes.

The linearized wavespeed associated with this specific parameter configuration was $c \approx 0.395$. Thus for only a slightly smaller value of the zonal flow parameter ω, the linearized and associated non-linear wavespeeds would be very close to zero, so that the Rossby wave would be approximately stationary with respect to the surface of the Earth. We conjecture that the particular nature of the wavespeed–amplitude relationship for stationary Rossby waves would not be dissimilar to that computed for the case $\kappa = 4$ and $\omega = 1.0$. If this is so it would imply the existence of highly distorted nearly stationary Rossby waves containing high pressure ridges extending polewards from the equator, with cut-off low pressure cells in the mid-latitudes. This type of atmospheric configuration may offer a partial explanation for the instigation of certain types of atmospheric blocking events, with subsequent development of cut-off high-pressure cells near the mid-latitudes when full time dependence is included in the model. This conjecture is supported by previous work of Verkley [37,38] in which stationary modons in westerly background flows on a sphere are suggested as possible explanations for blocking events.

In this conjecture nothing is implied as to how the dynamical system moves from one solution branch to the next, nor is it expected that all the solution branches would be physically stable. However, if this proves to be true then the highly non-linear solutions calculated in this work would support the idea that some forms of

atmospheric blocking are primarily dynamical states which are accessible through appropriate forcing of the atmospheric system.

Acknowledgement

T.G.C. gratefully acknowledges the provision of an Australian Postgraduate Award which has enabled him the time to conduct this research as part of a PhD degree.

References

[1] C.G. Rossby, Relation between variations in the intensity of the zonal circulation of the atmosphere and the displacements of the semi-permanent centers of action, J. Marine Res. 2 (1939) 38–55.
[2] E. Lorenz, Barotropic instability of Rossby wave motion, J. Atmos. Sci. 29 (2) (1972) 258–265.
[3] D.K. Lilly, A note on barotropic instability and predictability, J. Atmos. Sci. 30 (1) (1973) 145–146.
[4] B. Haurwitz, The motion of atmospheric disturbances on the spherical earth, J. Marine Res. 3 (1940) 254–267.
[5] M.S. Longuet-Higgins, Planetary waves on a rotating sphere, Proc. R. Soc. Lond. A 279 (1964) 446–473.
[6] M.S. Longuet-Higgins, Planetary waves on a rotating sphere, II, Proc. R. Soc. Lond. A 284 (1965) 40–68.
[7] D.L. Williamson, J.B. Drake, J.J. Hack, R. Jakob, P.N. Swarztrauber, A standard test set for numerical approximations to the shallow water equations in spherical geometry, J. Comput. Phys. 102 (1992) 211–224.
[8] N.A. Phillips, Numerical integration of the primitive equations on the hemisphere, Mon. Weather Rev. 87 (1959) 333–345.
[9] J. Thuburn, Y. Li, Numerical simulations of Rossby–Haurwitz waves, Tellus A 52 (2000) 181–189.
[10] B.J. Hoskins, Stability of the Rossby–Haurwitz wave, Quart. J.R. Met. Soc. 99 (1973) 723–745.
[11] P.G. Baines, The stability of planetary waves on a sphere, J. Fluid Mech. 73 (part 2) (1976) 193–213.
[12] J.R. Wilton, On ripples, Philos. Mag. 29 (6) (1915) 688–700.
[13] L.W. Schwartz, J.-M. Vanden-Broeck, Numerical solution of the exact equations for capillary-gravity waves, J. Fluid Mech. 95 (1979) 119–139.
[14] S.J. Hogan, Some effects of surface tension on steep water waves, J. Fluid Mech. 91 (1979) 167–180.
[15] S.J. Hogan, Some effects of surface tension on steep water waves. Part 2, J. Fluid Mech. 96 (1980) 417–445.
[16] S.J. Hogan, Some effects of surface tension on steep water waves. Part 3, J. Fluid Mech. 110 (1981) 381–410.
[17] L.K. Forbes, Surface waves of large amplitude beneath an elastic sheet. Part 1. High-order series solution, J. Fluid Mech. 169 (1986) 409–428.
[18] L.K. Forbes, Surface waves of large amplitude beneath an elastic sheet. Part 2. Galerkin solution, J. Fluid Mech. 188 (1988) 491–508.
[19] M.S. Longuet-Higgins, A.E. Gill, Resonant interactions between planetary waves, Proc. R. Soc. Lond. A 299 (1967) 120–140.
[20] A.E. Gill, Atmosphere–Ocean Dynamics, Academic Press, 1982.
[21] R. Klein, Asymptotic analyses for atmospheric flows and the construction of asymptotically adaptive numerical methods, ZAMM Math. Mech. 80 (2000) 765–777.
[22] A. Kasahara, Effect of zonal flows on the free oscillations of a barotropic atmosphere, J. Atmos. Sci. 37 (5) (1980) 917–929.
[23] M. Van Dyke, Perturbation Methods in Fluid Mechanics, Parabolic Press, 1975.
[24] J. Pedlosky, Geophysical Fluid Dynamics, Springer-Verlag, 1982.
[25] M. Abramowitz, I.A. Stegun, Handbook of Mathematical Functions with Formulas, Graphs, and Mathematical Tables, Dover, 1972.
[26] D.R. Durran, Numerical Methods for Wave Equations in Geophysical Fluid Dynamics, Texts in Applied Mathematics, vol. 32, Springer-Verlag, 1998.
[27] W.H. Press, S.A. Teukolsky, W.T. Vetterling, B.P. Flannery, Numerical Recipes in C++: The Art of Scientific Computing, second ed., Cambridge University Press, 2002.
[28] W. Gander, W. Gautschi, Adaptive quadrature – revisited, BIT 40 (1) (2000) 84–101.
[29] J.P. Snyder, Map projections – a working manual, US Geological Survey Professional Paper, 1395, 1987.
[30] G.G. Stokes, On the theory of oscillatory waves, Camb. Trans. viii (1847) 441–473.
[31] L.W. Schwartz, Computer extension and analytic continuation of stokes' expansion for gravity waves, J. Fluid. Mech. 62 (1974) 553–578.
[32] E.D. Cokelet, Steep gravity waves in water of arbitrary uniform depth, Philos. Trans. R. Soc. London Ser. A 286 (1977) 183–230.
[33] L. Schwartz, J. Fenton, Strongly nonlinear waves, Ann. Rev. Fluid Mech. 14 (1982) 39–60.
[34] B. Chen, P. Saffman, Steady gravity-capillary waves on deep water II. Numerical results for finite amplitude, Stud. Appl. Math. 62 (1980) 95–111.
[35] B. Chen, P. Saffman, Numerical evidence for the existence of new types of gravity waves of permanent form on deep water, Stud. Appl. Maths 62 (1980) 1–21.
[36] W.F. Ames, Numerical Methods for Partial Differential Equations, second ed., Academic Press, 1977.
[37] W.T.M. Verkley, The construction of barotropic modons on a sphere, J. Atmos. Sci. 41 (16) (1984) 2492–2504.
[38] W.T.M. Verkley, Stationary barotropic modons in westerly background flows, J. Atmos. Sci. 44 (17) (1987) 2383–2398.